

# Optimized polarization state of transition dipole moment for chiral light-matter interactions

Jakub Rosiński,<sup>1</sup> Michał Gawętczyk,<sup>1</sup> Karol Tarnowski,<sup>2</sup> Paweł Karwat,<sup>3</sup> Daniel Wigger,<sup>3</sup> and Paweł Machnikowski<sup>1</sup>

<sup>1</sup>*Institute of Theoretical Physics, Wrocław University of Science and Technology, Wrocław, 50-370, Poland*

<sup>2</sup>*Department of Optics and Photonics, Wrocław University of Science and Technology, Wrocław, 50-370, Poland*

<sup>3</sup>*School of Physics, Trinity College Dublin, Dublin 2, Ireland*

(Dated: October 16, 2023)

Chiral coupling, enabling directional interactions between quantum dots (QDs) and photonic crystal waveguide modes, holds the promise for enhancing quantum information processing and communication. However, in epitaxial QD fabrication, the lack of precise control over lateral QD positions poses a challenge for achieving efficient chiral interfaces for large numbers of QDs. Conventionally, circularly polarized emitters are considered, but their directional emission area is rather small, leading to suboptimal overlap between highly directional emission and large Purcell enhancement regions. To address these limitations, we propose an innovative approach to engineering the elliptical polarization of the QD's transition dipole moment to facilitate an efficient chiral interface. By considering random QD positions, we demonstrate that realistic elliptical polarization significantly increases the effective directional coupling area, thereby improving the scalability of the device. Furthermore, an elliptically polarized emitter offers improved overlap between regions of high directionality and large Purcell enhancement. Our results present a viable path for efficient chiral coupling in QD-based photonic integrated circuits, bringing us closer to robust and scalable quantum networks with advanced quantum information storage, processing, and communication capabilities.

## I. INTRODUCTION

Applications in quantum information processing and quantum communication have attracted a lot of attention to quantum networks based on on-chip photonic integrated circuits [1–3]. A fundamental requirement for storing, processing, and exchanging information is to interface quantum nodes with quantum channels in such physical platforms [4–8]. This requires emitters that couple to photonic pathways, encoding the quantum information of a long-lived qubit onto a flying transporting qubit. On the one hand, in the past few years, several nanophotonic waveguide schemes have been proposed as channels, including photonic crystal waveguides (PCW) [9–11], optical fibers [12, 13], crossed- nanowire waveguides [14, 15], and nanobeam waveguides [16–18], which utilize quantum interfaces to transfer data from matter to photonic qubits. On the other hand, self-assembled semiconductor quantum dots (QDs) constitute an interesting class of emitters for photonic quantum technology applications [19, 20]. QDs may easily be integrated into photonic nanostructures since they are solid-state emitters and the spins in QDs have been identified as long-lived matter qubits [21–24].

In a QD-based implementation, quantum information has to be transferred to photonic channels by a controlled interface between the photonic propagating mode and the spin states of the QD. In a perfect world, such an interface would be deterministic, meaning that emission fully takes place into the desired mode, and the information is transmitted without information backflow or loss. Chiral interfaces that support directional interactions represent a promising paradigm for deterministically transferring the state of matter onto the quantum state of light, exploiting the direction-dependent nature of light-matter interaction [25]. The directional mode excitation arises from the longitudinal component of the electric field [26, 27] which, due to the  $\pm\pi/2$  phase shift with respect to the transverse field component, makes the polarization elliptical in the propagation plane. This polarization flips its

sign with the inversion of propagation direction due to the time-reversal symmetry of Maxwell's equations [28–30]. The chiral coupling emerges naturally in nanophotonic systems including plasmonic structures [31–33], crossed nanowire waveguides [14], whispering-gallery-mode resonators [34], dielectric nanobeam waveguides [15, 16], nanofibres [13, 35], and PCWs [9, 16, 36–38]. The coupling depends both on the polarization of the mode propagating in the photonic structure at the position of the emitter and on the polarization of the transition dipole moment of the emitter itself. In recent years PCWs have been demonstrated as promising structures offering the possibility to engineer the local polarization and dispersion [9, 10, 39–42]. On the other hand, there has been no attempt to optimize the coupling on the emitter side, in spite of the large flexibility of control over the optical properties of QDs offered by state-of-the-art manufacturing methods.

QDs are fabricated by epitaxial techniques, in which heterostructures are grown in individual layers [43–45]. The most common approach is the Stranski-Krastanov method, which relies on the self-assembly of a QD layer on a substrate surface due to the lattice mismatch of both layers. The main drawback of conventional growing techniques is the lack of precise control over the lateral positions of the QDs. One route to achieving control over QD location is based on the site-controlled growth of QDs [46–49]. However, the properties of such QDs, in terms of optical quality (emission linewidths and quantum efficiency) cannot match those of QDs based on the Stranski-Krastanow growth yet [50, 51]. As a viable alternative, nanophotonic structures can be aligned to a single QD that is first located by microscopy techniques [52–56]. However, such an integrated system cannot be scaled to more than a few QDs. Furthermore, nanofabrication protocols based on pre-located QDs allow for the emitter-photonic structure integration with an accuracy of around  $\delta \sim 35$  nm [57], limited by imperfections within the imaging system and the subsequent nanofabrication. This accuracy results in a precision spot with a radius  $\delta$  that is larger than the area of highly directional

emission by a circular dipole [16]. The restricted area of optimally directional coupling is a consequence of the fact that the guided mode is circularly polarized only in the close vicinity of a few points in each unit cell of the PCW (C points) [58], while elliptical polarization states predominate throughout the majority of the unit cell [39]. Moreover, a circularly polarized emitter offers a limited overlap between the areas of high directionality and large Purcell enhancement.

On the other hand, restricting the considerations to circular dipoles is an unnecessary limitation: In epitaxial nanostructures, the reduced symmetry of the confinement potential, which is influenced by in-plane geometry, strain anisotropy, or atomistic asymmetry leads to mixing between heavy and light holes in the valence band. As a result, the QD's bright electron-hole configurations are associated with elliptical dipoles [59] with typical degrees of linear polarization of 1%–20%. For excitonic transitions (recombination of an electron-hole pair), the two elliptically polarized states are coupled by electron-hole exchange with a relative phase locked by time reversal, leading to two linearly polarized transitions. Elliptical polarization can be restored by applying a magnetic field, offering a degree of control by exploiting the competition between the electron-hole exchange and Zeeman energies. For a trion transition (electron-hole recombination in the presence of the additional, resident carrier) the electron-hole exchange is suppressed due to the singlet configuration of the two identical carriers (electrons or holes) and the system shows two time-reversal-symmetric elliptical transitions, corresponding to the two spin orientations of the final single-particle state.

To overcome the limitations of a circular emitter for chiral coupling, we here propose an approach for the engineering of elliptical polarization of the transition dipole moment of the QD, which can lead to an efficient chiral interface. Because the elliptical polarization states predominate in a PCW, the elliptical polarization of the dipole transition moment will maximize the average directionality of the emission. Here, we take randomized QD positions into account and show that the optimized elliptical polarization enhances the area of the effective directional coupling, thus improving the scalability of the device. The feasibility of our approach is confirmed by quantitatively modeling the QD properties using the  $\mathbf{k} \cdot \mathbf{p}$  method. We show that the optimal polarization properties correspond to realistic compositional and morphological characteristics of the QD.

## II. MODEL

We study a coupled PCW-QD system that realizes both strong photon-emitter interaction and high directionality. In this section, we describe the model of the waveguide followed by the model of the QD and characterization of the coupling. We consider an exemplary type of compatible emitter: self-assembled InAs quantum grown in a quaternary AlGaInAs matrix [60], whose polarization properties can be widely tuned.

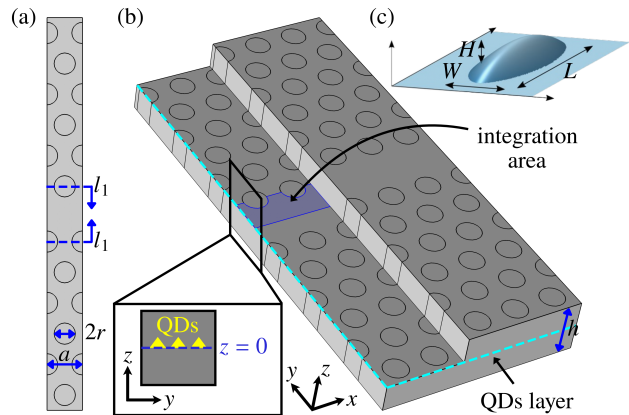


FIG. 1. (a) A unit cell of the PCW with the hexagonal lattice of air holes and an up-down glide-plane symmetry. The waveguide is described by the lattice constant  $a$ , the hole radius  $r$ , and the membrane thickness  $h$ . Additionally, the first row of holes is shifted by a distance  $l_1$ . (b) A view of the photonic structure showing the QD layer position ( $z = 0$ , indicated by the dashed blue line) and integration areas (highlighted in blue shading). (c) Schematic image of the QD geometry illustrating length  $L$ , width  $W$ , and height  $H$ .

### A. Waveguide

The geometry of the considered phononic crystal waveguide is presented in Fig. 1. The waveguide is created by a missing row of holes in a hexagonal pattern of air holes with equal radii  $r = 0.3a$ , a membrane thickness  $h = 0.64a$ , and a refractive index  $n = 3.35$ , where  $a$  denotes the lattice constant. Furthermore, one side of the waveguide is shifted by half a lattice constant along the propagation direction, leading to a glide plane waveguide structure. Such a symmetry breaking results in elliptically polarized light at the field maxima [9]. The structure is further modified by shifting the first rows of holes toward the waveguide's center by  $l_1 = a\sqrt{3}/20$ . While modifying the air hole diameter might bring additional advantages [61], it is less accurately realized in electron-beam lithography than changing their position. Therefore, we restrict the current study to structures with a fixed hole size. We design the waveguide to guide light with wavelengths near  $\lambda = 1550$  nm (0.8 eV), i.e., tuned for the third telecommunication window with the lowest optical-fiber losses. This is achieved by choosing the lattice constant  $a = 433$  nm. However, the studied waveguide design can be easily scaled [62] for use with any other quantum photonic platform.

We perform numerical finite element calculations using the commercial software COMSOL Multiphysics [63] to find the Bloch modes of the PCW and their eigenfrequencies. We apply Floquet boundary conditions in the propagation direction and periodic boundary condition in the  $y$  direction (Fig. 1b). We use an air layer of  $3h$  thickness and perfectly matched layers (PMLs) of  $1.5h$  thickness above and below the slab (in the  $z$  direction), where  $h$  is the thickness of the slab. We also introduced a perfect magnetic conductor (PMC) plane, oriented in the reflection symmetry plane of the waveguide

to limit the study to transverse electric (TE) modes and thus reduce the computational domain. We use a supercell of length  $a$  along the waveguide, width  $8.5a\sqrt{3} - 2l_1$ , and height  $5h$ , which is large enough to suppress interaction with neighboring supercells. The calculations utilize a grid with a maximum distance between the nearest mesh nodes of  $0.4a/n$ , where  $n$  is the refractive index of the domain. This mesh ensures that the eigenvalues converge with an accuracy of less than 0.1%.

Based on the amplitudes and phases for the components of the electric field, found from the simulations, we parameterize the in-plane part of the electric field as

$$\mathbf{e} = e_0 \begin{pmatrix} \cos(\chi_f) \cos(\Psi_f) - i \sin(\chi_f) \sin(\Psi_f) \\ \cos(\chi_f) \sin(\Psi_f) + i \sin(\chi_f) \cos(\Psi_f) \end{pmatrix}, \quad (1)$$

where  $e_0$  is the field amplitude, the angle  $0 \geq \Psi_f \geq \pi$  describes the orientation of the polarization ellipse and the angle  $-\pi/4 \geq \chi_f \geq \pi/4$  defines the degree of ellipticity, with  $\tan \chi_f = b/a$ , where  $a$  and  $b$  are the major and minor semi-axes, respectively, so that  $\chi_f = 0$  corresponds to linear polarizations,  $\chi_f = \pm\pi/4$  yields two opposite circular polarizations, and intermediate values of  $\chi_f$  correspond to elliptical polarization. More details concerning the parametrization can be found in Appendix A.

## B. Quantum dots

We consider a widely studied InAs/AlGaInAs self-assembled QD [59, 60, 64] emitting in the third telecom window centered at 1550 nm wavelength. Such QDs are characterized by a larger than typical in-plane size and asymmetry. The latter is defined by the lateral aspect ratio, which may vary from below 2 to about 10 [65]. The suitability of these QDs for the considered chiral interface results from the asymmetry-enabled mixing of heavy- and light-hole subbands, which leads to elliptically polarized transition dipoles [59] that can be controlled not only by the morphology of the structure but also by the magnetic field applied along the QD growth axis (Faraday geometry; perpendicular to the waveguide in our case).

For our modeling, we take a typical InAs/AlGaInAs QD [60] placed on a  $\sim 1$  nm thick InAs wetting layer. The QD has a triangular cross-section with a width-to-height ratio of  $W/H = 6$ . We vary  $H$  from 1.2 to 3 nm (as measured from the top of the wetting layer) and the length  $L$  from 20 to 60 nm in the simulation series, keeping other parameters fixed. We assume initially pure InAs in the QD and the wetting layer, and next, simulate the material interdiffusion at interfaces by performing Gaussian averaging of the three-dimensional material composition profile with the spatial extent  $\sigma = 0.9$  nm. The schematic picture in Fig. 1(c) shows a surface of constant indium concentration with corners smoothed by this averaging.

We minimize the elastic energy of the system within the theory of continuous elasticity on a uniform Cartesian grid to find the strain field. In a non-centrosymmetric material, the shear strain at the material interfaces induces a piezoelectric field, which we calculate to the second order in the strain-tensor elements. We use a state-of-the-art implementation [66] of

the multiband  $\mathbf{k} \cdot \mathbf{p}$  theory in the envelope function approximation [67] to find the eigenstates of electrons and holes in a QD. This calculation includes the strain, piezoelectric field, spin-orbit interaction, and external fields. The explicit form of the Hamiltonian can be found in Ref. [68], while details of the QD modeling and material parameters used are given in Ref. [64] and references therein. By numerically diagonalizing the Hamiltonian, we obtain the single-particle energy levels and carrier eigenstates as discretized pseudospinors of envelope functions for each subband.

We use the configuration-interaction approach to calculate exciton (bound electron-hole pair) and negative trion (two electrons and a hole) states with a configuration basis constructed of 24 electron and 24 hole states. Taking into account Coulomb interaction and phenomenological electron-hole exchange interaction, we obtain the exciton and trion eigenstates. Next, within the dipole approximation [69], we calculate interband optical transition dipole moments for the lowest-energy bright transitions as

$$\mathbf{d} = \sum_{jk} \frac{ie}{m_0(E_k - E_j)} c_{jk} \langle \Phi_j | \mathbf{P} | \Phi_k \rangle, \quad (2)$$

where  $m_0$  is the electron mass,  $\Phi_{j(k)}$  are eight-component pseudospinors of electron envelope functions for the  $j$ th valence ( $k$ th conduction) single-particle eigenstate spanned in the standard eight-band  $\mathbf{k} \cdot \mathbf{p}$  basis,  $c_{jk}$  are the coefficients for expansion of the exciton eigenstate in the electron-hole configuration basis, and  $\mathbf{P} = (m_0/\hbar)\partial H_{\mathbf{k}\cdot\mathbf{p}}/\partial \mathbf{k}$  is the momentum operator defined with respect to the  $\mathbf{k} \cdot \mathbf{p}$  Hamiltonian.

We consider a single, selected transition and hence assume the QD to be a two-level system. The in-plane part of the interband dipole moment characterizing the relevant transition in the QD is parametrized as

$$\mathbf{d} = d_0 \begin{pmatrix} \cos(\chi_d) \cos(\Psi_d) - i \sin(\chi_d) \sin(\Psi_d) \\ \cos(\chi_d) \sin(\Psi_d) + i \sin(\chi_d) \cos(\Psi_d) \end{pmatrix}, \quad (3)$$

consistently with the parameterization of the field polarization defined in Eq. (1), with  $d_0$  denoting the magnitude of the dipole moment and with the same geometrical interpretation of the parameters (see Appendix A).

## C. Coupling

The emission rate of the quantum emitter into a given eigenmode within the dipole approximation is given by

$$\gamma_{\pm\mathbf{k}} \propto |\mathbf{d}^* \cdot \mathbf{e}_{\pm\mathbf{k}}|^2, \quad (4)$$

where  $\mathbf{e}_{\pm\mathbf{k}}$  is the field in the mode with wave vector  $\mathbf{k}$ , guided in the  $\pm x$  direction, respectively. In the presence of a transverse field component,  $\mathbf{e}_{\mathbf{k}} \neq \mathbf{e}_{-\mathbf{k}}$ . Therefore, the emission rates into counter-propagating modes are in general not equal ( $\gamma_{\mathbf{k}} \neq \gamma_{-\mathbf{k}}$ ), resulting in a nonzero chirality factor defined as the normalized difference between the forward and backward emission rates

$$D = \frac{\gamma_{-\mathbf{k}} - \gamma_{\mathbf{k}}}{\gamma_{-\mathbf{k}} + \gamma_{\mathbf{k}}}. \quad (5)$$

As the light-matter coupling depends on the polarization state of the emitter, we are able to engineer this coupling by properly adjusting the latter by tuning the emitter parameters.

An important advantage of photonic crystals is that they can enhance the emission from a quantum emitter into a desired guided mode due to the broadband Purcell effect and strong suppression of the coupling to radiation modes by the photonic bandgap effect [70–74]. Only QDs that simultaneously exhibit chiral coupling and high Purcell enhancement may fully benefit from chiral quantum optics. The Purcell factor reads [75]

$$F_{\mathbf{k}}(\mathbf{r}) = \frac{3\pi c^2 a_{\mathbf{g}}(k)}{\omega_k^2 \sqrt{\varepsilon(\mathbf{r})}} |\hat{\mathbf{d}}^* \cdot \hat{\mathbf{e}}_{\mathbf{k}}(\mathbf{r})|^2, \quad (6)$$

where  $\hat{\mathbf{d}} = \mathbf{d}/d_0$ ,  $\hat{\mathbf{e}}_{\mathbf{k}} = \mathbf{e}_{\mathbf{k}}/\tilde{e}_{k0}$  with the normalization  $\tilde{e}_{k0} = \left[ \int_{\text{SC}} d^3\mathbf{r} \varepsilon(\mathbf{r}) |\mathbf{e}_{\mathbf{k}}(\mathbf{r})|^2 \right]^{1/2}$ ,  $\omega_k$  is the mode frequency,  $\varepsilon(\mathbf{r})$  is the relative electric permittivity at the point  $\mathbf{r}$ , and the group index for the considered mode is given by

$$n_g(k) = \frac{2c(U_{e,\mathbf{k}} + U_{h,\mathbf{k}})}{\left| \int_{\text{SC}} d^3\mathbf{r} \text{Re}[\mathbf{e}_{\mathbf{k}}^*(\mathbf{r}) \times \mathbf{h}_{\mathbf{k}}^*(\mathbf{r})] \right|}, \quad (7)$$

where  $c$  is the speed of light in vacuum,  $\mathbf{h}_{\mathbf{k}}$  is the magnetic field of the mode,  $V_{\text{SC}}$  is the PCW super-cell volume and  $U_{e,\mathbf{k}}(U_{h,\mathbf{k}})$  is the time-averaged electric (magnetic) field energy in the super-cell volume. As a consequence of enhancing the emission to a desired mode and suppression of the coupling to radiation modes, a near-unity efficiency of emission into the desired guided mode (the  $\beta$  factor) is achievable [76], even in the fast light regime [37], and it is remarkably robust to the position of the emitter in the waveguide [76].

To simulate the coupling of the propagation mode with a QD emitter at a random in-plane position for a given dipole polarization we assume every possible position of the QD within the waveguide core individually and integrate the directionality over that area. Since QDs cannot lie within the air holes, and efficient channeling to the defect mode requires a close distance of a QD to the defect region, we have restricted the integration area to the vicinity of the core region indicated by the blue shaded region in the Fig. 1(b). We consider half of the core region because the same coupling in the other half can be obtained by inverting all polarizations. Note that integration over the full core region formally always results in a vanishing average directionality. Furthermore, to suppress couplings with TM modes, we place the quantum emitter in the symmetry plane  $z = 0$  (dashed line in Fig 1(b)).

### III. RESULTS

#### A. Waveguide modes

Using the finite element method, we first determine the photonic TE-like bands, shown in Fig. 2(a), and the corresponding group indices [Fig. 2(b)] for the photonic crystal waveguide. The defect modes are plotted with solid lines, whereas the extended modes in the photonic crystal and the extended modes

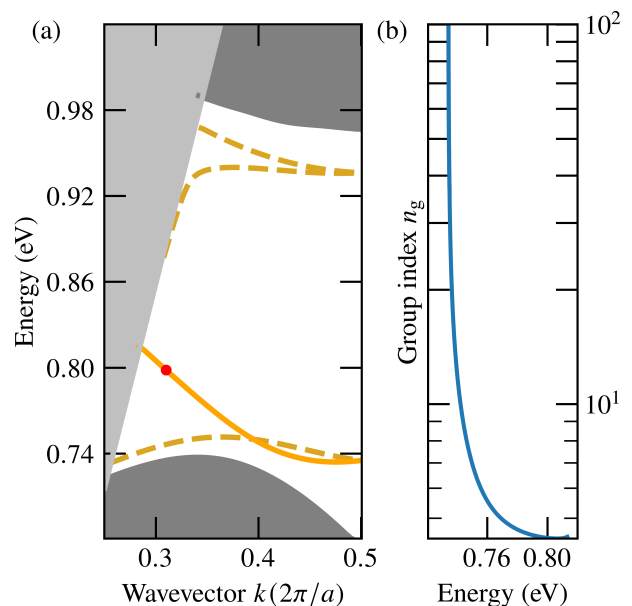


FIG. 2. Projected TE band structure of the PCW displaying waveguide modes (orange). The gray regions mark the membrane guided modes (dark gray) and radiation modes (light gray) that are not bound to the membrane. The solid line indicates the guided mode considered in our study, whereas the dashed curves represent other, potentially leaky modes. The chosen wavevector for further investigation is highlighted by the red dot. (b) Group index  $n_g$  of the considered guided mode as a function of mode energy.

propagating in the air (radiation modes) are represented as dark and light grey-shaded areas, respectively. The dashed curves represent other, potentially leaky modes near the continuum. We see that the chosen structure supports one well-confined mode. In addition, there are three modes near the bulk modes (dashed) that are anticipated to leak into the continuum in practice. The favorable guided mode (solid) spans a wide frequency range, which offers a good spectral adjustment to the QD line. In addition, it is a well-confined mode and is selected for further consideration.

Next, we calculate the polarization properties of the selected mode and extract the polarization parameters as described in Appendix A). We show the ellipticity angle  $\chi_f$  in the plane  $z = 0$  as a function of the position in Fig. 3(a) and the orientation angle  $\Psi_f$  in Fig. 3(b). We can clearly see in Fig. 3(a) that the two helicities (right-handed in green and left-handed in purple) almost exclusively appear in each half of the waveguide. While the white line in the plot indicates linear polarization, the singular very dark spots (highlighted by the red crosses, C points) mark circular polarization. Apart from these tiny regions in the waveguide center and close to the air holes, the selected mode shows predominantly elliptical polarization. This nicely illustrates the potential of elliptical polarization for a flexible device design. Figure 3(b) shows the orientation of the polarization ellipse. From the dominant dark colors, we find that in large areas of the waveguide, the orientation is along the propagation direction of the light.

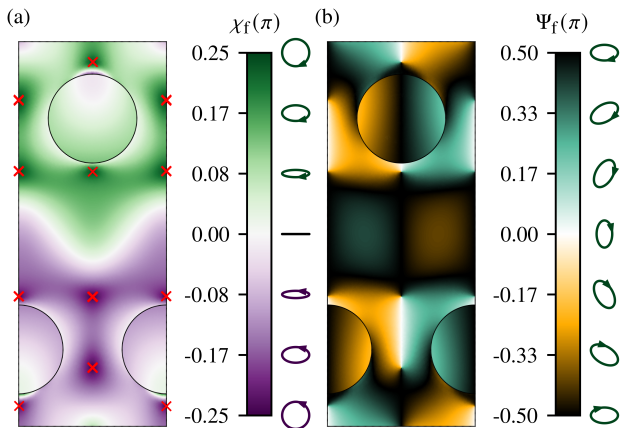


FIG. 3. Polarization ellipticity angle (a) and orientation angle (b) within the core area of the PCW unit cell, for selected guided mode in the  $z = 0$  plane for the considered mode. States having right- and left-handed ellipses are shown with green and purple, respectively. The red crosses in (a) indicate C points with circular polarization.

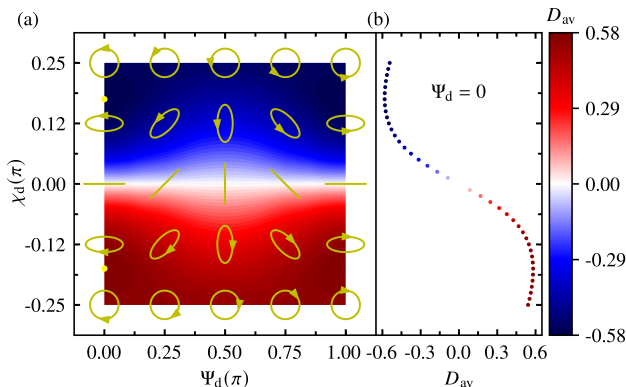


FIG. 4. (a) Map of the averaged directionality of the emission from a randomly placed QD as a function of the polarization of the transition dipole moment parametrized by orientation angle  $\Psi_d$  and ellipticity angle  $\chi_d$ . Yellow lines illustrate polarization states for a given  $\Psi_d$  and  $\chi_d$ , while the yellow dots indicate the maximum and minimum values of average directionality. (b) Cut line of the map in (a) for the orientation angle  $\Psi_d = 0$ .

## B. Emitter coupling

We now consider a QD emitter coupled to the electric field of the selected guided mode. In the first step, we treat the emitter formally, characterizing its polarization by the orientation and ellipticity angles  $(\Psi, \chi)$ . For every polarization state of the dipole transition moment, we calculate the directionality from Eq. (5) at a given point in the structure. In order to account for a random placement of the QD, we average the result over half the core region (blue shaded region in Fig. 1(b)), as discussed above. Figure 4 presents the main result, showing the averaged directionality of the QD emission for different polarization states of the dipole transition

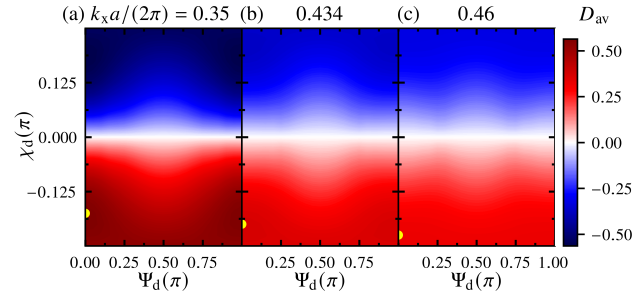


FIG. 5. Average directionality map of QDs with random in-plane spatial positioning, as in Fig. 4(a) for (a)  $k_x a / (2\pi) = 0.35$  ( $n_g \approx 4.85$ ), (b)  $k_x a / (2\pi) = 0.434$  ( $n_g \approx 15.1$ ), (c)  $k_x a / (2\pi) = 0.46$  ( $n_g \approx 46.8$ ). Yellow dots indicate the maximum values of average directionality.

moment of the QD for  $k_x a / (2\pi) = 0.31$  ( $n_g \approx 4.4$ ). The averaged directionality varies with both angles, reaching the maximum value of 0.58 for the optimal elliptical polarization with  $(\Psi_d, \chi_d) = (0, 0.145\pi)$  and zero for all linear polarizations. The optimal parameter values correspond to the dipole orientation  $\hat{d} = (0.898 - 0.0001i, 0.00028 + 0.44i)$ .

Interestingly, the average directionality decreases with increasing the group index. This is illustrated in Fig. 5, where we present the average directionality calculated for different wavevectors corresponding to different values of  $n_g$ . As the light slows down (from (a) to (c)), the maximum average directionality decreases and the optimal ellipticity angle tends to approach circular polarization. It is well-known that in-plane backscattering between the counter-propagating modes scales as  $n_g^2$  [77], leading to large losses in the slow light regime. Here, we choose the smallest possible group index, keeping the wavevector away from the light cone to prevent coupling the radiation modes.

We further calculate the directionality of emission  $D$  from Eq. (5) as a function of the emitter position, assuming the optimal transition dipole found above, as well as for the circular dipole for comparison, and mark the areas where  $|D| \geq 0.9$ . The calculated maps are shown in the left panels of Fig. 6(a) and 6(b) for the optimal dipole found above and for a circular dipole, respectively. In the left panels, the areas with  $|D| \geq 0.9$  are marked by red (right-handed) and blue (left-handed) colors, and we can directly see that in the case of elliptical polarization two large regions spread continuously through the entire unit cell in light propagation direction (Fig. 6(a)). In contrast, for circular polarization in Fig. 6(b) the areas form smaller isolated spots. To quantify this difference, the overall area is about 4 times larger for optimized elliptical polarization than the one where a circular dipole is assumed, and more than 6 times larger than  $A = \pi\xi^2$ , where  $\xi$  is the precision of embedding a QD in a photonic structure, which is  $\approx 40$  nm for InGaAs QD [57].

Optimizing the dipole moment is beneficial only if high directionality can be combined with efficient emission. Therefore, in the middle and right panels of Fig. 6, we present maps of the Purcell factor calculated from Eq. (6). Furthermore,

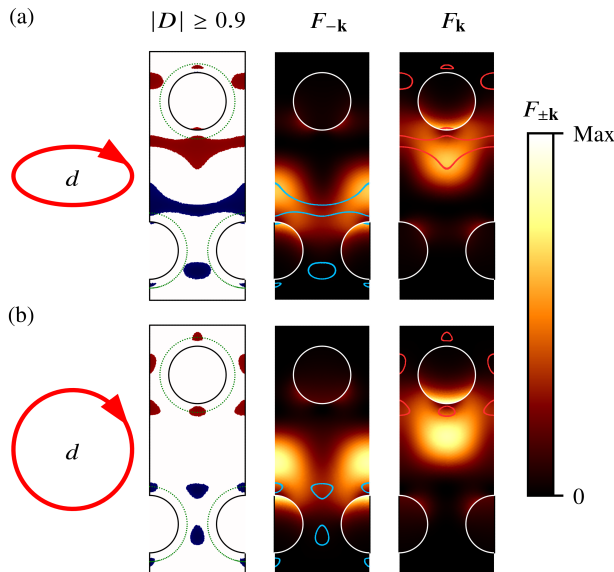


FIG. 6. Areas where  $|D| \geq 0.9$  (left) and Purcell factor (middle, right) for an optimized elliptical polarization state (a) and a circular one as a reference (b). In the left panels, the red areas indicate positive values of  $D$ , whereas blue ones denote negative values of  $D$ . The dotted green lines indicate a distance of 40 nm from the air-dielectric interfaces of the holes. In the middle and right panels the edge lines indicating the area where  $|D| \geq 0.9$  are plotted onto the Purcell maps to illustrate the overlap between these two quantities.

although the magnitude of the Purcell factor is slightly reduced for an elliptically polarized dipole (middle and right panel in Fig. 6(a)) as compared to the circular dipole (middle and right panel in Fig. 6(b)), the area of considerable Purcell enhancement remains essentially unchanged. As a result, the elliptical polarization yields a much more extended area where high directionality is combined with considerable Purcell enhancement (bright regions). Another benefit of elliptical polarization that can be observed in the directionality map is a small shift of high directionality regions away from the air-dielectric interfaces of the holes, which is desired to sustain good optical quality of the QD emitter and compatibility with the current technology: Etching the holes affects the near surrounding of the holes, which will alter the optical quality of the QDs in these areas. Therefore, a 40 nm range around the air hole, consistent with the current technology limitations [57] is marked with a dotted green line in Fig. 6 which shall be avoided in actual devices.

Finally, we show that the optimal value of the transition dipole is feasible only with neutral exciton within realistic QD technology. For a series of QDs described in Sec. II B with different geometrical parameters we calculate the single-particle, exciton and trion eigenstates, as well as their optical transition dipole moments. In Fig. 7, we present the analysis of the polarization properties of QDs, specifically focusing on the ellipticity angle of the transition dipole. In Fig. 7(a), we study the ellipticity angle as a function of QD width, for two values of the QD length and a fixed height-to-width ratio, showing results

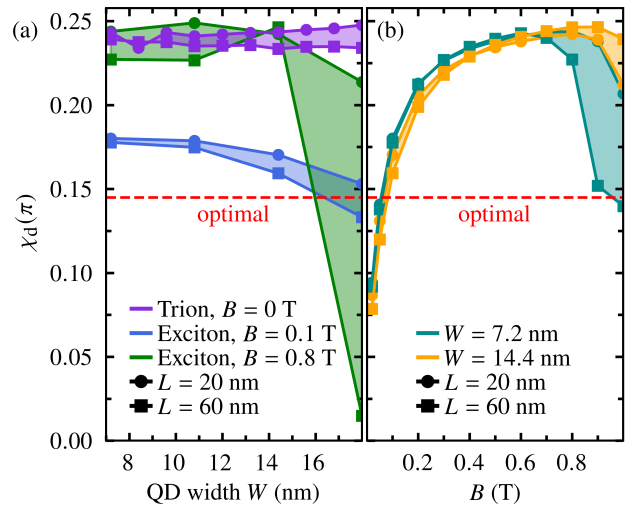


FIG. 7. (a) Ellipticity angle of the polarization of the dipole transition moment in a QD as a function of QD width, illustrating both the neutral exciton and trion (violet line). In the case of exciton two distinct regimes are shown: a low magnetic field regime (blue line) and a high magnetic field regime (green line). (b) Ellipticity angle of the polarization of the dipole transition moment in a QD as a function of applied magnetic field for neutral exciton. Results are presented for QDs of varying widths, with dark cyan representing small widths and orange for larger widths. In both (a) and (b), data are presented for QDs of two different lengths:  $L = 20$  nm (solid line with circle markers) and 60 nm (solid line with square markers). The red dashed line indicates the optimal ellipticity angle found in Fig. 4.

for both neutral excitons and trions. For excitons, our analysis reveals a noteworthy finding: we can achieve the optimal ellipticity angle in both weak and strong magnetic field regimes (blue and green curves in Fig. 7(a)) for QDs with larger widths. However, these ellipticity angles are not attainable with trions (violet curve in Fig. 7(a)). In Fig. 7(b), we further investigate the dependence of the ellipticity of the transition dipole on the applied magnetic field for neutral excitons. It is evident that neither the width nor the length of QDs significantly impacts the ellipticity angle when the magnetic field strength remains below 0.6 T. To achieve the situation in which the polarization of QD transition matches the optimized ellipticity (marked as a dashed red line) we find that a magnetic field of  $\approx 0.1$  T is sufficient for realistic QD lengths of a few tens of nm.

#### IV. CONCLUSIONS

In this study, we have explored the chiral coupling to enable directional interactions between quantum dots (QDs) and photonic crystal waveguide modes, with the aim to improve scalability for quantum information processing and communication. Our investigation focused on the challenges posed by the lack of precise control over lateral QD positions in epitaxial QD fabrication, which hinders the achievement of efficient chiral interfaces. By considering random QD positions, we have found that working with elliptical polarization significantly

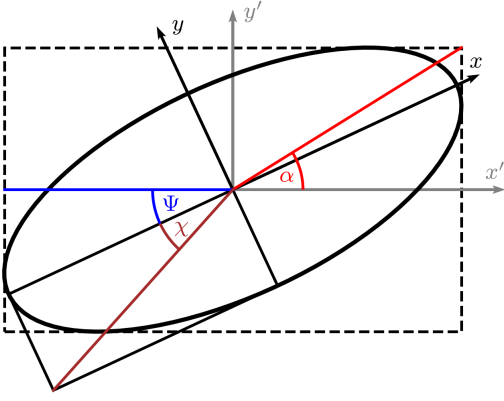


FIG. 8. An illustration of the polarization ellipse with indicated parametrization. The parameter  $\delta$  does not have a straightforward geometrical representation.

enhances the high directional contrast ( $|D| \geq 0.9$ ) area compared to circularly polarized emitters, thereby improving the scalability of the device. Furthermore, we have shown that an elliptically polarized emitter offers improved overlap between regions of high directionality and large Purcell enhancement, presenting an attractive solution for realizing efficient chiral coupling. These findings present an appealing and efficient solution for achieving robust chiral coupling in quantum dots-based photonic integrated circuits. Using the  $\mathbf{k} \cdot \mathbf{p}$  method, we have further revealed that the optimal polarization properties can be achieved within realistic compositional and morphological characteristics of QDs. Our study demonstrates that achieving the optimal value of the transition dipole moment is attainable exclusively with neutral excitons. Additionally, the examination of the ellipticity angle's dependence on the applied magnetic field for neutral excitons has shown that the width and length of QDs exert minimal influence on the ellipticity angle when the magnetic field strength remains below 0.6 T. This observation is particularly significant given the inherent limitations in accurately controlling QD sizes within the constraints of realistic QD technology. We have determined that a small magnetic field of approximately 0.1 T is sufficient to align the QD transition polarization with the optimized ellipticity angle. This demonstrates the feasibility of implementing engineered elliptical polarization in practical quantum technology applications, facilitating enhanced quantum information storage, processing, and communication capabilities. Additionally, this elliptical polarization in a QD does not require a significant out-of-plane magnetic field to prepare the QD spins into  $S_z = \pm 1$  states. This notable advantage further solidifies elliptically polarized emitters as the most efficient choice for chiral interactions, eliminating the need for complex and cumbersome preparation techniques.

#### ACKNOWLEDGMENTS

M.G. is grateful to K. Gawarecki for sharing his  $\mathbf{k} \cdot \mathbf{p}$  code. Part of the calculations has been carried out using resources provided by Wrocław Centre for Networking and Supercomputing (<http://wcss.pl>), Grant No. 203 and Grant No. 521.

D.W. acknowledges financial support of Science Foundation Ireland (SFI) under Grant numbers 18/RP/6236 and 22/PATH-S/10656.

#### Appendix A: Polarization Ellipse

A polarization state of a mode at a given point or of an optical transition dipole moment is described in terms of the geometrical parameters of the polarization ellipse. Two different parametrizations given by angle pairs  $\Psi, \chi$  and  $\alpha, \delta$  can be used [78] to describe the polarization. The meaning of those angles is shown in Fig. 8. The ellipticity angle  $\chi$  ( $-\pi/4 \geq \chi \geq \pi/4$ ) is defined as a ratio of the length of the semi-minor axis of the ellipse  $u$  to the length of its semi-major axis  $v$ , such that  $\tan(\chi) = u/v$ . The orientation (also known as tilt or azimuth angle)  $\Psi$  ( $-\pi/2 \geq \Psi \geq \pi/2$ ) is the angle between the major axis of the ellipse and the  $x$  axis defining the orientation of the ellipse in its plane.  $\delta = \delta_y - \delta_x$  ( $0 \geq \delta \geq 2\pi$ ) is the phase difference between two electric field components.  $\alpha$  ( $0 \leq \alpha \leq \pi/2$ ) is a diagonal (amplitude ratio) angle defined as  $\tan(\alpha) = e_{0y}/e_{0x}$ . The polarization is right-handed (RH) if the ellipse is traversed in a clockwise sense when looking against the propagation direction (looking "into the beam" - many optics textbooks use this convention instead of the convention assuming to look in the direction of the wave's propagation). Assuming a right-handed coordinate system and electromagnetic wave propagating in the  $z$ -direction a clockwise rotation corresponds to a RH polarization when we look into the page in Fig. 8. RH (LH) polarization corresponds to positive (negative) values of ellipticity angles.

From the simulation, we obtain the electric field amplitudes of mode  $e_{0x}$  and  $e_{0y}$ , as well as the phase difference  $\delta$  between them. Next, we calculate the Stokes parameters

$$\begin{aligned} S_0 &= e_{0x}^2 + e_{0y}^2, \\ S_1 &= e_{0x}^2 - e_{0y}^2, \\ S_2 &= 2e_{0x}e_{0y} \cos(\delta), \\ S_3 &= 2e_{0x}e_{0y} \sin(\delta). \end{aligned} \quad (\text{A1})$$

Finally, in the last step of our analysis, we determine the ellipticity  $\chi$  and orientation  $\Psi$  angle from the Stokes parameters

$$\begin{aligned} \chi &= 0.5 \arcsin(S_3/S_0), \\ \Psi &= 0.5 \arctan(S_2/S_1). \end{aligned} \quad (\text{A2})$$

Alternatively, the dipole can also be characterized using a second set of angle ( $\alpha, \delta$ )

$$\mathbf{d} = \begin{pmatrix} \cos(\alpha) \\ \sin(\alpha)e^{i\delta} \end{pmatrix}, \quad (\text{A3})$$

In this case, we can extract the ellipticity and orientation angle from the following relationship

$$\begin{aligned} \cos(2\alpha) &= \cos(2\chi) \cos(2\Psi), \\ \tan(\delta) &= \tan(2\chi)/\sin(2\Psi). \end{aligned} \quad (\text{A4})$$

- [1] J. L. O'Brien, A. Furusawa, and J. Vučković, Photonic quantum technologies, *Nat. Photonics* **3**, 687 (2009).
- [2] P. Lodahl, Quantum-dot based photonic quantum networks, *Quantum Sci. Technol.* **3**, 013001 (2017).
- [3] J. Wang, F. Sciarrino, A. Laing, and M. G. Thompson, Integrated photonic quantum technologies, *Nat. Photonics* **14**, 273 (2020).
- [4] J. I. Cirac, P. Zoller, H. J. Kimble, and H. Mabuchi, Quantum State Transfer and Entanglement Distribution among Distant Nodes in a Quantum Network, *Phys. Rev. Lett.* **78**, 3221 (1997).
- [5] W. Yao, R.-B. Liu, and L. Sham, Theory of control of the spin-photon interface for quantum networks, *Phys. Rev. Lett.* **95**, 030504 (2005).
- [6] S. Tanzilli, W. Tittel, M. Halder, O. Alibart, P. Baldi, N. Gisin, and H. Zbinden, A photonic quantum information interface, *Nature* **437**, 116 (2005).
- [7] S. Ritter, C. Nölleke, C. Hahn, A. Reiserer, A. Neuzner, M. Uphoff, M. Mücke, E. Figueroa, J. Bochmann, and G. Rempe, An elementary quantum network of single atoms in optical cavities, *Nature* **484**, 195 (2012).
- [8] N. Kalb, A. A. Reiserer, P. C. Humphreys, J. J. Bakermans, S. J. Kamerling, N. H. Nickerson, S. C. Benjamin, D. J. Twitchen, M. Markham, and R. Hanson, Entanglement distillation between solid-state quantum network nodes, *Science* **356**, 928 (2017).
- [9] I. Söllner, S. Mahmoodian, S. L. Hansen, L. Midolo, A. Javadi, G. Kiršanskė, T. Pregnolato, H. El-Ella, E. H. Lee, J. D. Song, S. Stobbe, and P. Lodahl, Deterministic photon-emitter coupling in chiral photonic circuits, *Nat. Nanotechnol.* **10**, 775 (2015).
- [10] A. B. Young, A. Thijssen, D. M. Beggs, P. Androvitsaneas, L. Kuipers, J. G. Rarity, S. Hughes, and R. Oulton, Polarization engineering in photonic crystal waveguides for spin-photon entanglers, *Phys. Rev. Lett.* **115**, 153901 (2015).
- [11] S. Mahmoodian, P. Lodahl, and A. S. Sørensen, Quantum networks with chiral-light-matter interaction in waveguides, *Phys. Rev. Lett.* **117**, 240501 (2016).
- [12] J. Petersen, J. Volz, and A. Rauschenbeutel, Chiral nanophotonic waveguide interface based on spin-orbit interaction of light, *Science* **346**, 67 (2014).
- [13] R. Mitsch, C. Sayrin, B. Albrecht, P. Schneeweiss, and A. Rauschenbeutel, Quantum state-controlled directional spontaneous emission of photons into a nanophotonic waveguide, *Nat. Commun.* **5**, 5713 (2014).
- [14] I. Luxmoore, N. Wasley, A. Ramsay, A. Thijssen, R. Oulton, M. Hugues, S. Kasture, V. Achanta, A. Fox, and M. Skolnick, Interfacing spins in an InGaAs quantum dot to a semiconductor waveguide circuit using emitted photons, *Phys. Rev. Lett.* **110**, 037402 (2013).
- [15] I. Luxmoore, N. A. Wasley, A. J. Ramsay, A. Thijssen, R. Oulton, M. Hugues, A. Fox, and M. Skolnick, Optical control of the emission direction of a quantum dot, *Appl. Phys. Lett.* **103**, 241102 (2013).
- [16] R. Coles, D. Price, J. Dixon, B. Royall, E. Clarke, P. Kok, M. Skolnick, A. Fox, and M. Makhonin, Chirality of nanophotonic waveguide with embedded quantum emitter for unidirectional spin transfer, *Nat. Commun.* **7**, 11183 (2016).
- [17] R. J. Coles, D. M. Price, B. Royall, E. Clarke, M. S. Skolnick, A. M. Fox, and M. Makhonin, Path-dependent initialization of a single quantum dot exciton spin in a nanophotonic waveguide, *Phys. Rev. B* **95**, 121401 (2017).
- [18] P. Mrowiński, P. Schnauber, P. Gutsche, A. Kaganskiy, J. Schall, S. Burger, S. Rodt, and S. Reitzenstein, Directional emission of a deterministically fabricated quantum dot-bragg reflection multimode waveguide system, *ACS Photonics* **6**, 2231 (2019).
- [19] H. Wang, J. Qin, X. Ding, M.-C. Chen, S. Chen, X. You, Y.-M. He, X. Jiang, L. You, Z. Wang, *et al.*, Boson sampling with 20 input photons and a 60-mode interferometer in a 1 0 14-dimensional hilbert space, *Physical review letters* **123**, 250503 (2019).
- [20] J. Loredó, M. Broome, P. Hilaire, O. Gazzano, I. Sagnes, A. Lemaitre, M. Almeida, P. Senellart, and A. White, Boson sampling with single-photon fock states from a bright solid-state source, *Physical review letters* **118**, 130503 (2017).
- [21] A. Imamoglu, D. D. Awschalom, G. Burkard, D. P. DiVincenzo, D. Loss, M. S. Sherwin, and A. Small, Quantum information processing using quantum dot spins and cavity QED, *Phys. Rev. Lett.* **83**, 4204 (1999).
- [22] R. J. Warburton, Single spins in self-assembled quantum dots, *Nat. Mater.* **12**, 483 (2013).
- [23] J. Yoneda, K. Takeda, T. Otsuka, T. Nakajima, M. R. Delbecq, G. Allison, T. Honda, T. Kodera, S. Oda, Y. Hoshi, N. Usami, K. M. Itoh, and S. Tarucha, A quantum-dot spin qubit with coherence limited by charge noise and fidelity higher than 99.9%, *Nat. Nanotechnol.* **13**, 102 (2018).
- [24] J. C. Norman, D. Jung, Y. Wan, and J. E. Bowers, Perspective: The future of quantum dot photonic integrated circuits, *APL photonics* **3**, 030901 (2018).
- [25] P. Lodahl, S. Mahmoodian, S. Stobbe, A. Rauschenbeutel, P. Schneeweiss, J. Volz, H. Pichler, and P. Zoller, Chiral quantum optics, *Nature* **541**, 473 (2017).
- [26] M. Lax, W. H. Louisell, and W. B. McKnight, From Maxwell to paraxial wave optics, *Phys. Rev. A* **11**, 1365 (1975).
- [27] K. Y. Bliokh and F. Nori, Transverse spin of a surface polariton, *Phys. Rev. A* **85**, 061801 (2012).
- [28] K. Y. Bliokh and F. Nori, Transverse and longitudinal angular momenta of light, *Phys. Rep.* **592**, 1 (2015).
- [29] K. Y. Bliokh, F. J. Rodríguez-Fortuño, F. Nori, and A. V. Zayats, Spin-orbit interactions of light, *Nat. Photonics* **9**, 796 (2015).
- [30] A. Aiello, P. Banzer, M. Neugebauer, and G. Leuchs, From transverse angular momentum to photonic wheels, *Nat. Photonics* **9**, 789 (2015).
- [31] S.-Y. Lee, I.-M. Lee, J. Park, S. Oh, W. Lee, K.-Y. Kim, and B. Lee, Role of magnetic induction currents in nanoslit excitation of surface plasmon polaritons, *Phys. Rev. Lett.* **108**, 213907 (2012).
- [32] F. J. Rodríguez-Fortuño, G. Marino, P. Ginzburg, D. O'Connor, A. Martínez, G. A. Wurtz, and A. V. Zayats, Near-field interference for the unidirectional excitation of electromagnetic guided modes, *Science* **340**, 328 (2013).
- [33] J. Lin, J. B. Mueller, Q. Wang, G. Yuan, N. Antoniou, X.-C. Yuan, and F. Capasso, Polarization-controlled tunable directional coupling of surface plasmon polaritons, *Science* **340**, 331 (2013).
- [34] C. Junge, D. O'shea, J. Volz, and A. Rauschenbeutel, Strong coupling between single atoms and nontransversal photons, *Phys. Rev. Lett.* **110**, 213604 (2013).
- [35] C. Sayrin, C. Junge, R. Mitsch, B. Albrecht, D. O'Shea, P. Schneeweiss, J. Volz, and A. Rauschenbeutel, Nanophotonic optical isolator controlled by the internal state of cold atoms, *Phys. Rev. X* **5**, 041036 (2015).
- [36] B. Le Feber, N. Rotenberg, and L. Kuipers, Nanophotonic control of circular dipole emission, *Nat. Commun.* **6**, 6695 (2015).
- [37] L. Scarpelli, B. Lang, F. Masia, D. Beggs, E. Muljarov, A. Young, R. Oulton, M. Kamp, S. Höfling, C. Schneider, and

- W. Langbein, 99% beta factor and directional coupling of quantum dots to fast light in photonic crystal waveguides determined by spectral imaging, *Phys. Rev. B* **100**, 035311 (2019).
- [38] N. V. Hauff, H. Le Jeannic, P. Lodahl, S. Hughes, and N. Rotenberg, Chiral quantum optics in broken-symmetry and topological photonic crystal waveguides, *Phys. Rev. Res.* **4**, 023082 (2022).
- [39] M. Burrelli, R. Engelen, A. Opheij, D. van Oosten, D. Mori, T. Baba, and L. Kuipers, Observation of polarization singularities at the nanoscale, *Phys. Rev. Lett.* **102**, 033902 (2009).
- [40] S. Mahmoodian, K. Prindal-Nielsen, I. Söllner, S. Stobbe, and P. Lodahl, Engineering chiral light-matter interaction in photonic crystal waveguides with slow light, *Optical Materials Express* **7**, 43 (2017).
- [41] B. Lang, R. Oulton, and D. M. Beggs, Optimised photonic crystal waveguide for chiral light-matter interactions, *Journal of Optics* **19**, 045001 (2016).
- [42] D. M. Beggs, B. Lang, and R. Oulton, Optimised chiral light-matter interactions at polarisation singularities for quantum photonics, in *2017 19th International Conference on Transparent Optical Networks (ICTON)* (IEEE, 2017) pp. 1–4.
- [43] V. A. Shchukin and D. Bimberg, Spontaneous ordering of nanostructures on crystal surfaces, *Reviews of Modern Physics* **71**, 1125 (1999).
- [44] J. Stangl, V. Holý, and G. Bauer, Structural properties of self-organized semiconductor nanostructures, *Reviews of modern physics* **76**, 725 (2004).
- [45] G. Biasiol and S. Heun, Compositional mapping of semiconductor quantum dots and rings, *Physics Reports* **500**, 117 (2011).
- [46] C. Schneider, M. Strauß, T. Süner, A. Huggenberger, D. Wiener, S. Reitzenstein, M. Kamp, S. Höfling, and A. Forchel, Lithographic alignment to site-controlled quantum dots for device integration, *Appl. Phys. Lett.* **92**, 183101 (2008).
- [47] C. Schneider, A. Huggenberger, T. Süner, T. Heindel, M. Strauß, S. Göpfert, P. Weinmann, S. Reitzenstein, L. Worschech, M. Kamp, *et al.*, Single site-controlled in (ga) as/gaas quantum dots: growth, properties and device integration, *Nanotechnology* **20**, 434012 (2009).
- [48] J. Skiba-Szymanska, A. Jamil, I. Farrer, M. B. Ward, C. A. Nicoll, D. J. Ellis, J. P. Griffiths, D. Anderson, G. A. Jones, D. A. Ritchie, *et al.*, Narrow emission linewidths of positioned inas quantum dots grown on pre-patterned gaas (100) substrates, *Nanotechnology* **22**, 065302 (2011).
- [49] K. Jons, P. Atkinson, M. Muller, M. Heldmaier, S. Ulrich, O. Schmidt, and P. Michler, Triggered indistinguishable single photons with narrow line widths from site-controlled quantum dots, *Nano Letters* **13**, 126 (2013).
- [50] F. Albert, S. Stobbe, C. Schneider, T. Heindel, S. Reitzenstein, S. Höfling, P. Lodahl, L. Worschech, and A. Forchel, Quantum efficiency and oscillator strength of site-controlled inas quantum dots, *Applied Physics Letters* **96** (2010).
- [51] A. Huggenberger, S. Heckelmann, C. Schneider, S. Höfling, S. Reitzenstein, L. Worschech, M. Kamp, and A. Forchel, Narrow spectral linewidth from single site-controlled in (ga) as quantum dots with high uniformity, *Applied Physics Letters* **98** (2011).
- [52] A. Badolato, K. Hennessy, M. Atature, J. Dreiser, E. Hu, P. M. Petroff, and A. Imamoglu, Deterministic coupling of single quantum dots to single nanocavity modes, *Science* **308**, 1158 (2005).
- [53] K. Hennessy, A. Badolato, M. Winger, D. Gerace, M. Atature, S. Gulde, S. Fält, E. L. Hu, and A. Imamoglu, Quantum nature of a strongly coupled single quantum dot-cavity system, *Nature* **445**, 896 (2007).
- [54] A. Dousse, L. Lanco, J. Suffczyński, E. Semenova, A. Miard, A. Lemaître, I. Sagnes, C. Roblin, J. Bloch, and P. Senellart, Controlled light-matter coupling for a single quantum dot embedded in a pillar microcavity using far-field optical lithography, *Physical review letters* **101**, 267404 (2008).
- [55] S. M. Thon, M. T. Rakher, H. Kim, J. Gudat, W. T. Irvine, P. M. Petroff, and D. Bouwmeester, Strong coupling through optical positioning of a quantum dot in a photonic crystal cavity, *Applied Physics Letters* **94**, 111115 (2009).
- [56] T. Kojima, K. Kojima, T. Asano, and S. Noda, Accurate alignment of a photonic crystal nanocavity with an embedded quantum dot based on optical microscopic photoluminescence imaging, *Applied Physics Letters* **102**, 011110 (2013).
- [57] T. Pregolato, X.-L. Chu, T. Schröder, R. Schott, A. D. Wieck, A. Ludwig, P. Lodahl, and N. Rotenberg, Deterministic positioning of nanophotonic waveguides around single self-assembled quantum dots, *APL Photonics* **5**, 086101 (2020).
- [58] B. Lang, D. M. Beggs, A. B. Young, J. G. Rarity, and R. Oulton, Stability of polarization singularities in disordered photonic crystal waveguides, *Phys. Rev. A* **92**, 063819 (2015).
- [59] A. Musiał, P. Kaczmarkiewicz, G. Sęk, P. Podemski, P. Machnikowski, J. Misiewicz, S. Hein, S. Höfling, and A. Forchel, Carrier trapping and luminescence polarization in quantum dashes, *Phys. Rev. B* **85**, 035314 (2012).
- [60] A. Sauerwald, T. Kümmell, G. Bacher, A. Somers, R. Schwertberger, J. P. Reithmaier, and A. Forchel, Size control of InAs quantum dashes, *Appl. Phys. Lett.* **86**, 253112 (2005).
- [61] S. Schulz, L. O’Faolain, D. M. Beggs, T. P. White, A. Melloni, and T. F. Krauss, Dispersion engineered slow light in photonic crystals: a comparison, *Journal of Optics* **12**, 104004 (2010).
- [62] J. D. Joannopoulos, P. R. Villeneuve, and S. Fan, Photonic crystals, *Solid State Communications* **102**, 165 (1997).
- [63] *Comsol multiphysics*, <https://www.comsol.com/>.
- [64] M. Gawelczyk, M. Syperek, A. Maryński, P. Mrowiński, Ł. Dusanowski, K. Gawarecki, J. Misiewicz, A. Somers, J. P. Reithmaier, S. Höfling, and G. Sęk, Exciton lifetime and emission polarization dispersion in strongly in-plane asymmetric nanostructures, *Phys. Rev. B* **96**, 245425 (2017).
- [65] W. Rudno-Rudziński, R. Kudrawiec, P. Podemski, G. Sęk, J. Misiewicz, A. Somers, R. Schwertberger, J. P. Reithmaier, and A. Forchel, Photorefractance-probed excited states in InAs/InGaAlAs quantum dashes grown on InP substrate, *Appl. Phys. Lett.* **89**, 031908 (2006).
- [66] K. Gawarecki, P. Machnikowski, and T. Kuhn, Electron states in a double quantum dot with broken axial symmetry, *Phys. Rev. B* **90**, 085437 (2014).
- [67] T. B. Bahder, Eight-band k-p model of strained zinc-blende crystals, *Phys. Rev. B* **41**, 11992 (1990).
- [68] A. Mielnik-Pyszczorski, K. Gawarecki, M. Gawelczyk, and P. Machnikowski, Dominant role of the shear strain induced admixture in spin-flip processes in self-assembled quantum dots, *Phys. Rev. B* **97**, 245313 (2018).
- [69] J. Andrzejewski, G. Sęk, E. O’Reilly, A. Fiore, and J. Misiewicz, Eight-band k-p calculations of the composition contrast effect on the linear polarization properties of columnar quantum dots, *J. Appl. Phys.* **107**, 073509 (2010).
- [70] V. P. Bykov, Spontaneous emission from a medium with a band spectrum, *Quantum Electron.* **4**, 861 (1975).
- [71] P. Lodahl, A. Floris van Driel, I. S. Nikolaev, A. Irman, K. Overgaag, D. Vanmaekelbergh, and W. L. Vos, Controlling the dynamics of spontaneous emission from quantum dots by photonic crystals, *Nature* **430**, 654 (2004).
- [72] E. Yablonoitch, Inhibited spontaneous emission in solid-state physics and electronics, *Phys. Rev. Lett.* **58**, 2059 (1987).

- [73] Q. Wang, S. Stobbe, and P. Lodahl, Mapping the local density of optical states of a photonic crystal with single quantum dots, *Phys. Rev. Lett.* **107**, 167404 (2011).
- [74] A. F. Koenderink, M. Kafesaki, C. M. Soukoulis, and V. Sandoghdar, Spontaneous emission rates of dipoles in photonic crystal membranes, *J. Opt. Soc. Am. B* **23**, 1196 (2006).
- [75] S. Hughes, Enhanced single-photon emission from quantum dots in photonic crystal waveguides and nanocavities, *Opt. Lett.* **29**, 2659 (2004).
- [76] M. Arcari, I. Söllner, A. Javadi, S. L. Hansen, S. Mahmoodian, J. Liu, H. Thyrestrup, E. H. Lee, J. D. Song, S. Stobbe, and P. Lodahl, Near-Unity Coupling Efficiency of a Quantum Emitter to a Photonic Crystal Waveguide, *Phys. Rev. Lett.* **113**, 093603 (2014).
- [77] S. Hughes, L. Ramunno, J. F. Young, and J. Sipe, Extrinsic optical scattering loss in photonic crystal waveguides: role of fabrication disorder and photon group velocity, *Physical review letters* **94**, 033903 (2005).
- [78] D. H. Goldstein, *Polarized light* (CRC press, 2017).